

## RESEARCH ARTICLE SUMMARY

## STRUCTURAL BIOLOGY

# Structure of the human PKD1-PKD2 complex

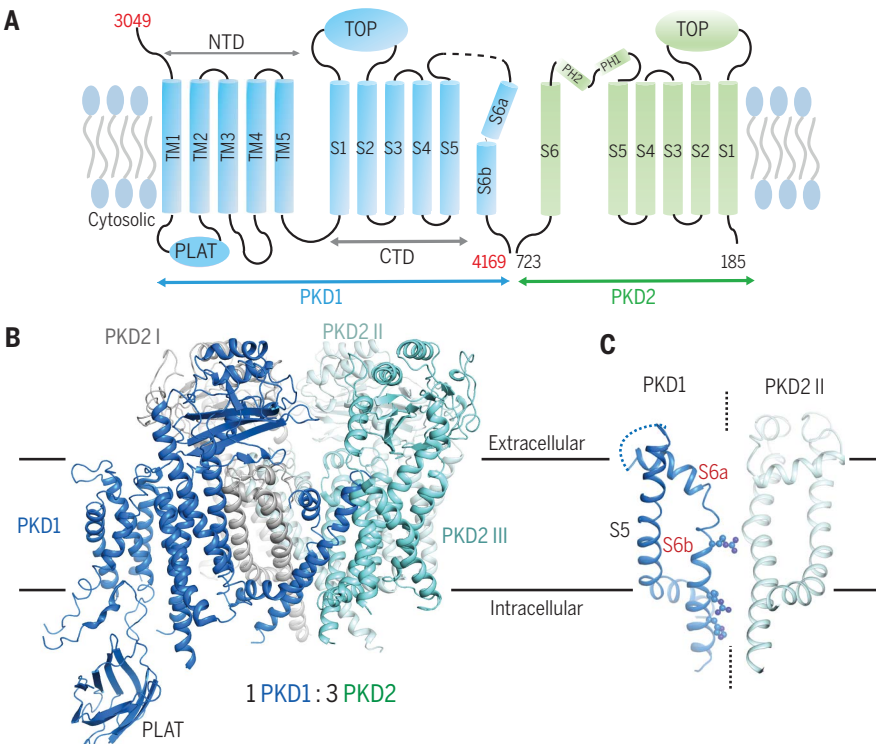
Qiang Su\*, Feizhuo Hu\*, Xiaofei Ge, Jianlin Lei, Shengqiang Yu, Tingliang Wang, Qiang Zhou, Changlin Mei, Yigong Shi†

**INTRODUCTION:** Mutations in two genes, *PKD1* and *PKD2*, are responsible for about 85 and 10% of all cases of autosomal dominant polycystic kidney disease (ADPKD), one of the most common monogenetic disorders. However, the physiological and pathophysiological functions of the gene products polycystin-1 and polycystin-2 (PC1 and PC2, also known as PKD1 and PKD2) are not well understood.

PKD1, which comprises 4303 residues, may serve as a receptor that senses chemical and mechanical force stimuli, whereas PKD2, whose homotetrameric structure conforms to a typical

group II transient receptor potential (TRP) channel, is hypothesized to be an endoplasmic reticulum  $\text{Ca}^{2+}$ -release channel and regulate intracellular  $\text{Ca}^{2+}$  concentrations. The two proteins were predicted to coexist as a heterooligomer on primary cilia in the renal epithelium, although the molecular basis for the formation of this complex remains elusive.

**RATIONALE:** To investigate the assembly of PKD1 and PKD2, we sought to resolve the structure of the PKD1-PKD2 complex. After extensive screening for optimal constructs and expres-



## Cryo-EM structure of the truncated human PKD1-PKD2 complex at 3.6-Å resolution.

(A) Topological illustration of PKD1 and PKD2. NTD, N-terminal domain; TOP, also known as the polycystin domain; CTD, C-terminal domain (which includes S1 to S6 and the TOP domain). (B) The 1:3 organization of the PKD1-PKD2 complex. PKD2 I, II, and III are the three PKD2 subunits. (C) Unconventional conformation of the S6 segment in PKD1. The sequences between the S5 and S6 segments are flexible and disordered in PKD1. The extracellular segment of the bent S6 resembles PH1.

sion systems, a homogeneous complex was obtained through coexpression of FLAG-tagged PKD1 and Twin-Strep-tagged PKD2 (hereafter referred to as PKD1 and PKD2 for simplicity). Approximately 100 µg of the complex was obtained through affinity purification and size exclusion chromatography from 40 to 50 liters of suspension human embryonic kidney (HEK) 293F cells. The structure of the complex was determined to 3.6-Å resolution with single-particle cryo-electron microscopy (cryo-EM).

**RESULTS:** PKD1 and PKD2 exhibit a 1:3 ratio in the structure. PKD1 consists of a voltage-gated ion channel (VGIC) fold

### ON OUR WEBSITE

Read the full article at <http://dx.doi.org/10.1126/science.aat9819>

that interacts with PKD2 to complete a domain-swapped TRP architecture. Several features, however, distinguish PKD1 from a canonical TRP channel. The S6 segment of PKD1 is broken in the middle, with the extracellular half, S6a, resembling pore helix 1 (PH1) in a typical VGIC. The sequence between S5 and S6a is highly flexible and disordered in the EM map. Three positively charged residues—Arg<sup>4100</sup>, Arg<sup>4107</sup>, and His<sup>4111</sup>—protrude into the putative ion-conducting path, likely impeding permeability of the  $\text{Ca}^{2+}$  ion. Therefore, the current structure may represent a potentially nonconductive state.

A discretely folded domain, which contains five transmembrane helices (TMs) and a cytosolic PLAT (polycystin-1, lipoxygenase, and alpha toxin) domain, precedes the VGIC fold in PKD1. The extracellular TOP domain of PKD1, which is frequently targeted for mutations in ADPKD, deviates from the expected symmetric position by 15°, leaving a gap in the extracellular TOP ring. Compared to the homotypic interactions among PKD2 subunits, the weakened interface between PKD1 and PKD2 provides a clue to the 1:3 stoichiometry in the heterotetramer. A higher ratio of PKD1 in the complex may weaken the association of the TOP domains.

**CONCLUSION:** The structure of the truncated PKD1-PKD2 complex reveals the molecular mechanism for the assembly of a hetero-oligomeric complex and provides a physical basis for mapping and understanding a large number of disease mutations. Elucidation of the functional mechanism of PKD1 and PKD2 as well as the disease mechanism of the hundreds of ADPKD mutations await further investigations. Our structure serves as a framework for future biophysical, biochemical, cellular, and computational analysis of PKD1-PKD2 and ADPKD. ■

The list of author affiliations is available in the full article online.

\*These authors contributed equally to this work.

†Corresponding author. Email: shi-lab@tsinghua.edu.cn (Y.S.)  
Cite this article as Q. Su *et al.*, *Science* **361**, eaat9819 (2018). DOI: 10.1126/science.aat9819

## RESEARCH ARTICLE

## STRUCTURAL BIOLOGY

# Structure of the human PKD1-PKD2 complex

Qiang Su<sup>1\*</sup>, Feizhuo Hu<sup>1\*</sup>, Xiaofei Ge<sup>1</sup>, Jianlin Lei<sup>2</sup>, Shengqiang Yu<sup>3</sup>, Tingliang Wang<sup>1,4</sup>, Qiang Zhou<sup>1</sup>, Changlin Mei<sup>3</sup>, Yigong Shi<sup>1,4†</sup>

Mutations in two genes, *PKD1* and *PKD2*, account for most cases of autosomal dominant polycystic kidney disease, one of the most common monogenetic disorders. Here we report the 3.6-angstrom cryo-electron microscopy structure of truncated human PKD1-PKD2 complex assembled in a 1:3 ratio. PKD1 contains a voltage-gated ion channel (VGIC) fold that interacts with PKD2 to form the domain-swapped, yet noncanonical, transient receptor potential (TRP) channel architecture. The S6 helix in PKD1 is broken in the middle, with the extracellular half, S6a, resembling pore helix 1 in a typical TRP channel. Three positively charged, cavity-facing residues on S6b may block cation permeation. In addition to the VGIC, a five-transmembrane helix domain and a cytosolic PLAT domain were resolved in PKD1. The PKD1-PKD2 complex structure establishes a framework for dissecting the function and disease mechanisms of the PKD proteins.

**A**utosomal dominant polycystic kidney disease (ADPKD) is a potentially lethal monogenic disorder that manifests in renal disease and, in some cases, abnormalities in the liver, pancreas, brain, or arterial blood vessels (1). ADPKD is typically diagnosed in adults with an incidence of 1:400 to 1:1000 and affects about 6 million people worldwide (2). The hallmarks of the disease are bilateral, fluid-filled, enlarged renal cysts, which increase in number with age (3). Mutations in two genes, *PKD1* and *PKD2*, whose products are polycystin-1 and polycystin-2 (PC1 and PC2, also known as PKD1 and PKD2), account for about 85 and 10% of all ADPKD cases, respectively (2, 4–8). Despite extensive effort, the physiological and pathophysiological mechanisms of PKD1 and PKD2 are not well understood.

PKD1 may function as a receptor that senses both chemical and mechanical force stimuli and regulates cytosolic cyclic adenosine monophosphate (cAMP) concentrations and downstream signaling (6, 9–12). PKD2 is hypothesized to be an endoplasmic reticulum Ca<sup>2+</sup>-release channel and regulate intracellular Ca<sup>2+</sup> concentrations (13). In addition, PKD2 (colocalizes) with PKD1 on the shaft and basal body of primary cilia in the renal epithelium (14–16) and may contribute

to fluid-flow sensation (11). Coexpression of human PKD1 and PKD2 is reported to produce distinct cation currents in Chinese hamster ovary cells (17). However, the channel activity of the ciliary PKD1-PKD2 complex is controversial. Delling *et al.* recently reported a complete lack of mechanically induced calcium influxes at physiological or supraphysiological levels of fluid flow against primary cilia (18).

Equally controversial is the molecular basis for the hetero-oligomerization of the PKD1-PKD2 complex. PKD1 and PKD2 were suggested to interact through their C-terminal coiled-coil domains (19–22). Other experiments, in which the complex was preserved in the absence of the coiled-coil domains, implied that complex formation may require the N-terminal loops (23–25). However, the cryo-electron microscopy (cryo-EM) structures of homotetrameric PKD2 and PKD2-like 1 protein (PKD2L1) revealed oligomerization in the absence of the coiled-coil domains or N-terminal loops (4, 26). Furthermore, truncation of both the N- and C-terminal soluble domains of PKD2L1 did not alter the function of the PKD1L3-PKD2L1 complex, suggesting that these two elements are dispensable for hetero-oligomerization (26).

To elucidate the assembly of PKD1 and PKD2, we sought to resolve the structure of the PKD1-PKD2 complex. Several structures of PKD2 and related proteins in distinct states have been reported (4, 26–28). In addition to the typical transient receptor potential (TRP) or voltage-gated ion channel (VGIC) transmembrane fold, each protomer contains an extracellular domain between the S1 and S2 segments that constitutes the TOP domain (also known as the polycystin domain), a feature shared by group II TRP channels (29). In contrast to the structural advances for PKD2, the only structural information on PKD1 is a nuclear magnetic resonance structure of a

78-residue PKD domain (residues 275 to 353) (30). The 4303-residue human PKD1 comprises an N-terminal extracellular region, 11 transmembrane helices (TMs), and a C-terminal coiled-coil domain (6). The extracellular segments form multiple domains involved in cell-cell or cell-matrix interactions (7). The transmembrane region can be divided into two entities: the N-terminal transmembrane domain (NTMD) containing five TMs and the C-terminal transmembrane domain (CTMD) that conforms to the VGIC fold (6). Within the NTMD, TM1 and TM2 are separated by a so-called PLAT (polycystin-1, lipoxigenase, and alpha toxin) domain (Fig. 1A). The highly conserved PLAT domain may participate in lipid binding and trafficking (31, 32). Here we report the near-atomic-resolution cryo-EM structure of the complex between truncated human PKD1 and PKD2 in a closed conformation.

## Results

### Purification and structural determination of the PKD1-PKD2 complex

The bottleneck for structural elucidation of the PKD1-PKD2 complex was the expression and purification of homogeneous protein samples. To enhance biochemical stability, we screened numerous combinations of various constructs for both PKD1 and PKD2. Eventually, the complex obtained through coexpression of PKD1 residues 3049 to 4169 (PKD1<sup>3049–4169</sup>) and PKD2<sup>185–723</sup> (hereafter referred to as PKD1 and PKD2 for simplicity), in which the putative flexible regions at the N and C termini of both proteins were removed (27), exhibited optimal solution behavior. Importantly, similar to full-length proteins, PKD1<sup>3049–4169</sup> is targeted to the cell surface only when coexpressed with PKD2<sup>185–723</sup> (fig. S1) (33).

The final yield of this complex was ~100 µg from 40 to 50 liters of suspension human embryonic kidney (HEK) 293F cell culture. To purify this low-yield protein complex, triple FLAG tag and Twin-Strep-tag were attached to the N-termini of PKD1 and PKD2, respectively (fig. S2A). After tandem affinity purification, PKD1 and PKD2 were monitored by Coomassie blue staining of SDS-polyacrylamide gel electrophoresis (PAGE) and verified by Western blotting and mass spectrometric (MS) analysis (fig. S2, B and C). After the last step of size exclusion chromatography purification, during which PKD1 and PKD2 co-migrated, the peak fractions were pooled and concentrated for cryo-EM analysis (Fig. 1, B to D).

Details of sample preparation, data acquisition, and structural refinement can be found in the materials and methods. A total of 27,296 selected particles yielded a three-dimensional (3D) EM reconstruction at an overall resolution of 3.6 Å, according to the gold-standard Fourier shell correlation 0.143 criterion (34) (figs. S3 and S4). During local search 3D classification, the core region in the PKD1 subunit and two PKD2 subunits appeared more stable than the rest of the complex in some classes (fig. S4). We thereby combined these classes for further classification. Eventually 116,485 particles were selected to give rise to a map in which the resolution of

<sup>1</sup>Beijing Advanced Innovation Center for Structural Biology, Tsinghua-Peking Joint Center for Life Sciences, School of Life Sciences, School of Medicine, Tsinghua University, Beijing 100084, China. <sup>2</sup>Technology Center for Protein Sciences, Ministry of Education Key Laboratory of Protein Sciences, School of Life Sciences, Tsinghua University, Beijing 100084, China. <sup>3</sup>Department of Nephrology, Changzheng Hospital, Second Military Medical University, Shanghai 200433, China. <sup>4</sup>Institute of Biology, Westlake Institute for Advanced Study, Westlake University, 18 Shilongshan Road, Xihu District, Hangzhou 310064, Zhejiang Province, China.  
\*These authors contributed equally to this work.  
†Corresponding author. Email: shi-lab@tsinghua.edu.cn (Y.S.)

this core region was improved to 3.2 Å (fig. S4 and table S1).

### The “1 + 3” assembly of PKD1 and PKD2

The overall structure of the complex has dimensions of approximately 130 Å by 110 Å by 130 Å (Fig. 2A and fig. S5A). The transmembrane region of the complex comprises 29 TMs made up of two groups, the classical 24 TMs of an intact VGIC and 5 additional TMs. This organization is equivalent to a PKD2 homotetramer plus an NTMD of PKD1, confirming the presence of one PKD1 and three PKD2 (fig. S5B). The 1:3 stoichiometric ratio of PKD1 to PKD2 is consistent with single-molecule characterization of the full-length complex (21, 22). Quantitative MS analysis also confirmed that the stoichiometry of the truncated PKD1-PKD2 complex is largely consistent with that of full-length proteins (35–37) (table S2).

To facilitate illustration, the 11 TMs in PKD1 will be described as TM<sub>1</sub><sup>PKD1</sup> to TM<sub>5</sub><sup>PKD1</sup> and S<sub>1</sub><sup>PKD1</sup> to S<sub>6</sub><sup>PKD1</sup>. A β-barrel PLAT domain between TM<sub>1</sub><sup>PKD1</sup> and TM<sub>2</sub><sup>PKD1</sup> was resolved on the cytosolic side below the NTMD. The NTMD and PLAT are together described as the N-terminal domain (NTD) (Figs. 1A and 2B). Similar to PKD2, S<sub>1</sub><sup>PKD1</sup> to S<sub>4</sub><sup>PKD1</sup> constitute the voltage sensor-like domain (VSD<sup>PKD1</sup>), and the sequence between S1 and S2 forms the extracellular TOP<sup>PKD1</sup> domain (Fig. 2B) (4, 27). The three PKD2 subunits are referred to as I, II, and III following a clockwise order in the extracellular view (Fig. 2A and fig. S5, A and B).

Most segments in the PKD1-PKD2 complex were well resolved in the map (fig. S5, C to E), enabling assignment of ~800 side chains for the VGIC region on the basis of the structure of PKD2 and a PKD2-derived PKD1 homologous model. An initial model for the NTD of PKD1, predicted by the I-TASSER (iterative threading assembly refinement) server (38), fit well into the corresponding EM map. The boundaries of the TMs in PKD1 are largely consistent with those derived from hydrophobic predictions (table S3).

### A distinctive S6 segment in PKD1

The three PKD2 protomers in the complex remain nearly identical to those in the PKD2 homotetramer (Fig. 3A and fig. S6, A and B). The fourfold symmetry of the pore domain (PD) in the PKD1-PKD2 complex is broken, owing to the distinct conformation of the S<sub>6</sub><sup>PKD1</sup> segment (Fig. 3A and fig. S6B). The S<sub>6</sub><sup>PKD1</sup> segment is bent in the middle, a feature that has not been observed in any other structures of VGIC-fold channels (39–41). The two halves, designated as S6a and S6b, form an axial angle of ~120° in the middle of the membrane (Fig. 3A, middle, and fig. S5D). Intriguingly, the conformation and position of the S6a segment are reminiscent of those of pore helix 1 (PH1) in a canonical TRP channel (Fig. 3A, right, and fig. S6B) (29), whereas the sequences corresponding to the putative selectivity filter (SF) and the supporting pore helices (PH1 and PH2) are invisible in PKD1 (Fig. 3A, middle, and fig. S6, B and C). Although the flexibility of this segment prevents detailed

analysis, the conformation of S6a suggests that PKD1 may lack PH1, and also possibly lack a SF, when it is complexed with PKD2.

Another feature distinguishing S<sub>6</sub><sup>PKD1</sup> from a typical VGIC or TRP channel is that it contains three cavity-facing, positively charged residues—Arg<sup>4100</sup>, Arg<sup>4107</sup>, and His<sup>4111</sup>. These basic residues would be expected to disfavor cation penetration (Fig. 3B and fig. S6D), suggesting a potentially nonconductive state of the present structure. Arg<sup>4100</sup> is stabilized by the neighboring Phe<sup>669</sup> and Asn<sup>674</sup> on S6 of PKD2 I (S6<sub>I</sub>), and Arg<sup>4107</sup> and His<sup>4111</sup> interact with the polar residues Asn<sup>681</sup> and Asp<sup>682</sup> on S6<sub>I</sub> (Fig. 3B). The electrostatic interactions between S6b<sup>PKD1</sup> and S6<sub>I</sub> may provide the molecular basis for the 15° deviation of S<sub>6</sub><sup>PKD1</sup> from the expected position on the basis of four-fold symmetry (Fig. 3C). Residue Arg<sup>4100</sup> in PKD1 is highly conserved among different species, suggesting a critical role in the function of PKD1 (fig. S6C).

### The structure of NTD<sup>PKD1</sup>

A Dali (42) search suggests that the PKD1-NTMD represents a previously uncharacterized fold, in which the five TMs form a helical bundle and TM1 and TM2 are separated in the primary sequence by the PLAT domain (Fig. 4A). TM2 is preceded by a membrane reentrant loop (hereafter referred to as the pre-TM2 loop), which inserts into the cavity of the five-TM helical bundle, with a highly conserved Trp<sup>3263</sup> interacting with

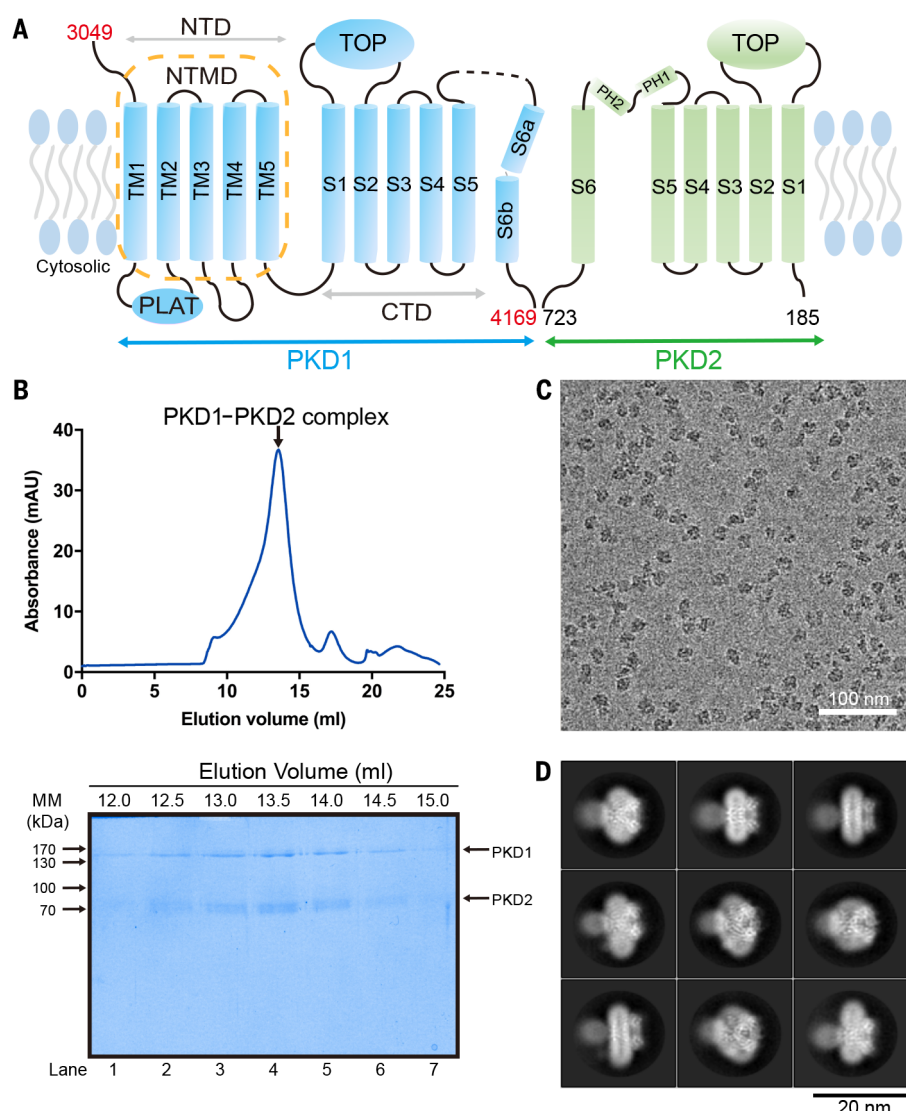


**Fig. 1. Expression and purification of the human PKD1-PKD2 complex.** (A) Topological illustration of PKD1 and PKD2. (B) Purification of the PKD1-PKD2 complex. Shown is a representative size exclusion chromatogram of the PKD1-PKD2 complex. The indicated peak fractions were resolved on SDS-PAGE and visualized by Coomassie blue staining. The smearable bands corresponding to PKD2 resulted from heterogeneous glycosylation. mAU, milli-arbitrary units. (C) Representative cryo-EM micrograph of the complex. MM, molecular mass. (D) 2D class averages of the complex.

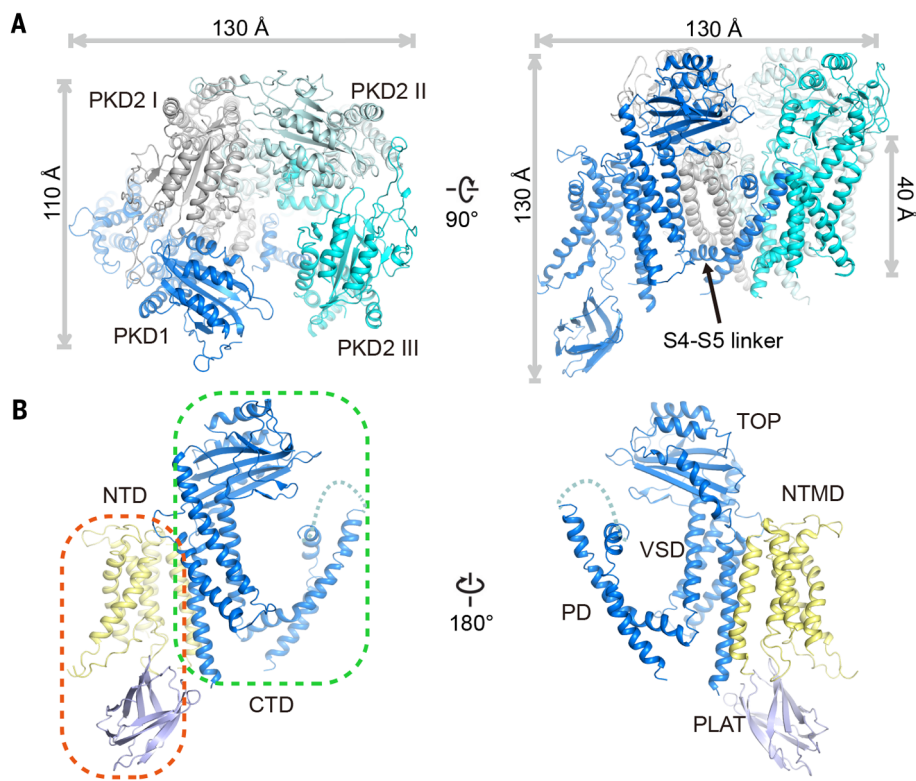


**Fig. 2. The “1 + 3” organization of the PKD1 and PKD2 complex.** (A) Overall structure of the complex. PKD1 is colored blue and the three PKD2 subunits are colored silver, pale cyan, and cyan. Two perpendicular views are shown. All structure figures were prepared in PyMol (70). (B) Structure of PKD1<sup>3049-4169</sup>. Two opposing side views are shown, and the protomer is domain colored.

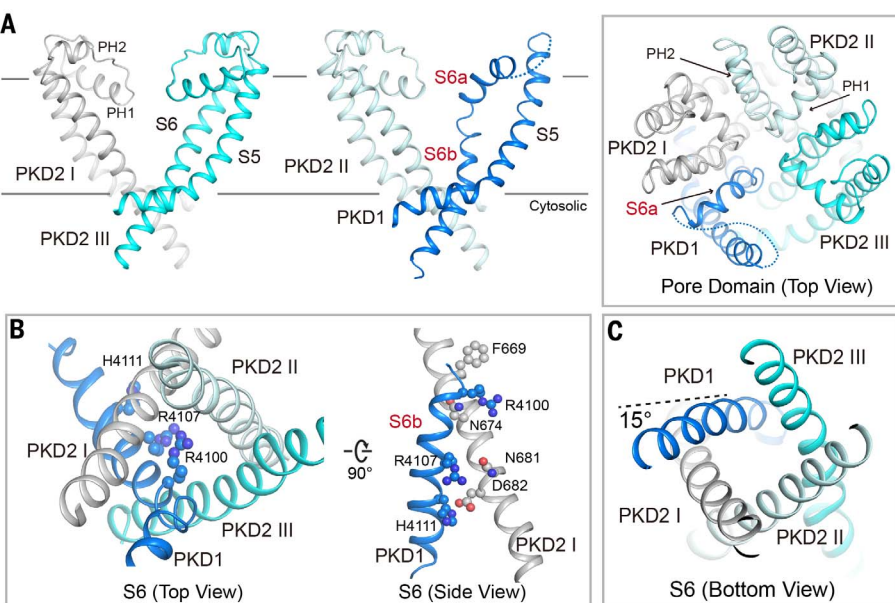


**Fig. 3. Conformation of the S6<sup>PKD1</sup> segment.** (A) PKD1 disrupts the fourfold symmetry of an otherwise typical VGIC fold. PKD1-S6 exhibits a distinct conformation from all VGIC channels of known structures. Whereas the sequences corresponding to the selectivity filter and the supporting helices (PH1 and PH2) are invisible in PKD1, the extracellular segment of the bent S6 resembles PH1. (B) Three positively charged residues on S6b<sup>PKD1</sup> may block cation permeation. Right: The conformation of S6b<sup>PKD1</sup> is stabilized by residues on PKD2-S6. The discussed residues are shown as spheres. (C) When viewed from the cytosolic side, S6<sup>PKD1</sup> displays a 15° deviation from the expected position for a fourfold symmetry.

Phe<sup>3596</sup> and Phe<sup>3600</sup> on TM5 (Fig. 4B and fig. S7A). This hydrophobic core may stabilize the overall conformation of the pre-TM2 loop. Missense mutation Trp<sup>3263</sup>→Arg (W3263R) has been identified as a highly likely pathogenic mutation of ADPKD (43), perhaps because it is important for the structural integrity of NTMD. The interface between NTD and VSD<sup>PKD1</sup> is constituted by hydrophobic residues on TM1 and S1 of PKD1 (Fig. 4C).

The four VSDs in the complex exhibit a pseudo fourfold symmetry. The conformations of the three VSDs from PKD2 are nearly identical (Fig. 4C and fig. S7B), whereas the overall structure of VSD<sup>PKD1</sup> resembles that of the VSD<sup>PKD2</sup> with minor variations. Compared to the corresponding segments in the VSDs of PKD2, the S2<sup>PKD1</sup> and S3<sup>PKD1</sup> segments move further away from the PD, whereas S1<sup>PKD1</sup> and S4<sup>PKD1</sup> shift toward the pore (fig. S7C). From the cytosolic view, the four helices in VSD<sup>PKD1</sup> undergo a counterclockwise irislike rotation compared to those in VSD<sup>PKD2</sup>, resulting in a larger intracellular mouth of the VSD<sup>PKD1</sup> (fig. S7C). Whereas the S3 and S4 segments are connected by a short helix in PKD2, the linker helix becomes an extended fragment of S3 in PKD1, similar to that in the open-state structure of PKD2L1 (fig. S7C) (26).

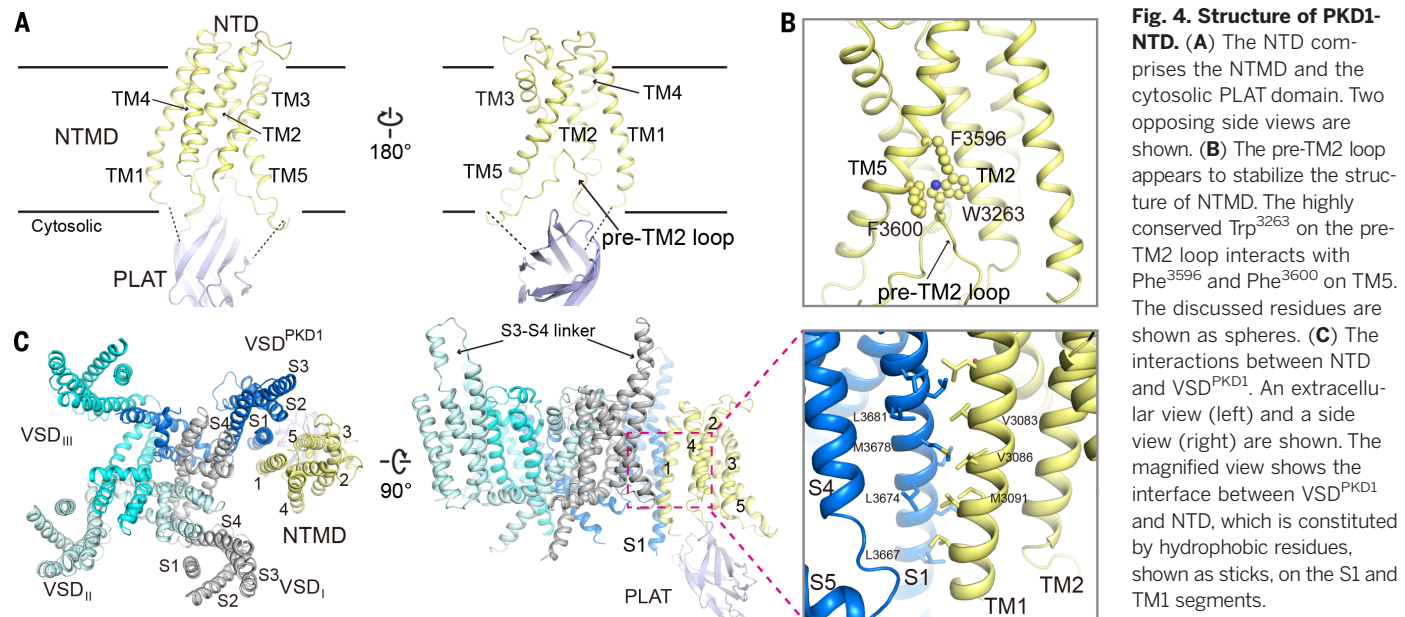
### Interactions between PKD1 and PKD2

The TOP domain in each protomer participates in the oligomerization of the homotetrameric PKD2 and PKD2L1 channels (4, 26, 27). By contrast, TOP<sup>PKD1</sup> deviates by ~15° from the expected symmetric position relative to the three TOP<sup>PKD2</sup> domains (Fig. 5A). When TOP<sup>PKD1</sup> is superimposed on any TOP<sup>PKD2</sup>, several structural distinctions are observed (Fig. 5B).

The most evident variation comes from the lack of the luminal loop from PKD1, which is missing in both the primary sequence and the 3D structure (fig. S8A) (44). In addition, the three-leaf clover (TLC) (27), also known as the finger 1 (4) motif, is invisible in the EM map of PKD1, likely owing to the flexibility of this region (Fig. 5B). The TLC is a critical element mediating the interactions of adjacent subunits in PKD2. The invisibility of TLC<sup>PKD1</sup> may indicate the lack of stable interaction between TOP<sup>PKD1</sup> and TOP<sub>III</sub>, consistent with the 15° deviation of TOP<sup>PKD1</sup>. On the other end, the TLC of TOP<sub>I</sub> retains interaction with TOP<sup>PKD1</sup>, an interface that is essential for complex assembly and trafficking (45) (fig. S8B).

The lack of a TLC<sup>PKD1</sup>-mediated interface between PKD1 and PKD2 may provide a tentative clue to the 1:3 assembly of the heterotetramer. A higher ratio of PKD1 in the complex would lead to decreased association of the TOP domains, disfavoring higher occupancy of PKD1. Supporting the structural analysis, TOP<sup>PKD1</sup> did not support homo-oligomerization of PKD1 in a co-immunoprecipitation assay (45).

The assembly of the PKD1-PKD2 complex involves two additional interfaces below the TOP domains. One is mediated by the electrostatic interaction between Arg<sup>3700</sup> on TOP<sup>PKD1</sup> and

**Fig. 4. Structure of PKD1-NTD.**

(A) The NTD comprises the NTMD and the cytosolic PLAT domain. Two opposing side views are shown. (B) The pre-TM2 loop appears to stabilize the structure of NTMD. The highly conserved Trp<sup>3263</sup> on the pre-TM2 loop interacts with Phe<sup>3596</sup> and Phe<sup>3600</sup> on TM5. The discussed residues are shown as spheres. (C) The interactions between NTD and VSD<sup>PKD1</sup>. An extracellular view (left) and a side view (right) are shown. The magnified view shows the interface between VSD<sup>PKD1</sup> and NTD, which is constituted by hydrophobic residues, shown as sticks, on the S1 and TM1 segments.

Downloaded from https://www.science.org at University of Georgia on August 19, 2024

Asp<sup>624</sup> on the linker of S6 and PH2 in PKD2 I, and the other is the canonical VGIC contacts constituted by hydrophobic residues in VSD<sup>PKD1</sup> and PD<sub>I</sub> (Fig. 5, C to E). The interfaces between adjacent PKD2 subunits in the hetero-oligomer are nearly identical to those in the homotetrameric PKD2 or PKD2L1 (fig. S8C) (26).

## Discussion

Structural determination of the PKD1-PKD2 complex affords the opportunity to map a large number of disease mutations (Fig. 6). Patients with mutations in PKD1 usually show more severe symptoms than those with mutations in PKD2 (2). The pathological mutations are unevenly distributed in PKD1, with the NTD and TOP domains being two hotspots (Fig. 6, left). The function of the NTD, a domain that is missing in PKD2 or other TRP channels, remains largely unknown except for limited characterizations of several disease mutations. Mutation R3277C in the NTMD has been suggested to affect the folding, glycosylation, and trafficking of PKD1 (46). Mutation R3162C in PLAT or W414G in TOP<sup>PKD2</sup> abrogates proper trafficking of PKD1 or PKD2, respectively (25, 31). A few disease-related residues are mapped to the hydrophobic interior. Substitution of these hydrophobic residues with charged ones—such as C3081R, W3726R, and L3834R—may destroy the structural integrity of NTMD and TOP<sup>PKD1</sup> (43, 47–52) (Fig. 6 and fig. S9A). Therefore, incorrect folding or trafficking of the PKD1-PKD2 complex can be pathogenic.

An unexpected observation is the lack of pathological mutations on the pore-forming segments in PKD1 (Fig. 6). Considering the distinct conformation of S6<sup>PKD1</sup>, we compared the sequence of S6<sup>PKD1</sup> with that in different PKD1 and PKD2 homologs (fig. S9B). S6<sup>PKD1</sup> is the only one that contains multiple positively charged residues. In the present structure, these residues—Arg<sup>4100</sup>, Arg<sup>4107</sup>, and His<sup>4111</sup>—protrude into the potential

ion-conducting path, likely leading to poor, if any, ion permeability (4, 53, 54) (Fig. 3B and fig. S5D). By contrast, the S6 segments in PKD1L3, PKD2L1, and PKD2, which share sequence similarity, are enriched in hydrophobic residues, a common feature found in most TRP and VGIC channels (fig. S9B). The ion conduction of PKD2L1 and the hetero-oligomer between PKD1L3 and PKD2L1 can be recorded easily (4, 26). Notably, several likely neutral mutations implicated in disease have been mapped to the S6<sup>PKD1</sup> or PD<sup>PKD1</sup>, indicating that the pathogenic mechanism of PKD1 may be independent of a putative ion-conducting activity (43, 48, 55, 56).

PKD1 and PKD2 are hypothesized to form a complex in the primary cilia (11, 57). Recent electrophysiological characterizations on the renal collecting duct epithelium suggested that PKD2 could function as a monovalent cation-selective channel and that the ciliary ion conductance is independent of PKD1 (53, 58). The structural features are consistent with the observation that PKD1 may be irrelevant to the ciliary ion current.

The near-atomic-resolution structure of the PKD1-PKD2 complex reveals the molecular details of the assembly of a hetero-oligomeric complex and provides the template for mapping a large number of disease mutations. Elucidation of the functional mechanism of PKD1 and PKD2 as well as the disease mechanism of the hundreds of ADPKD mutations await further investigations. Our structure serves as a framework for future biophysical, biochemical, cellular, and computational analysis of PKD1-PKD2 and ADPKD.

## Materials and methods

### Transient protein expression and purification

The codon-optimized full-length cDNAs for human PKD1 and PKD2 were synthesized by Tsingke

Company (hPKD1 [Uniprot: P98161-1]; hPKD2 [Uniprot: Q13563-1]). For structural analysis, the truncated constructs of PKD1 (residues 3049 to 4169) with N-terminal triple FLAG tag (DYKDHGDYKDHDIDYKDDDK) and PKD2 (residues 185 to 723) with N-terminal Twin-Strep-Tag II (WSHPQFEKGGGGSGGGSGSAWSHPQFEK) from IBA GmbH were subcloned into the pcAG vector (59). For mass spectrometric (MS) analysis, the FLAG tag (DYKDDDDK) and Twin-Strep-tag II were fused at the C terminus of human full-length PKD1 and N terminus of human full-length PKD2, respectively (60, 61). For immunofluorescence experiments, the FLAG tag is fused at its N terminus after the PKD1's signal peptide (MPPAAPARLALALGLGLWLGA). The sequences of all constructs were verified before cell expression and protein purification.

The HEK 293F cells (Invitrogen) were cultured in SMM 293T-I medium (Sino Biological Inc.) at 37°C supplemented with 5% CO<sub>2</sub> in a Multitron-Pro shaker (Infors) at 130 rpm. When cell density reached 2 × 10<sup>6</sup> to 2.5 × 10<sup>6</sup> cells per ml, the cells were cotransfected with equal mass amount of the plasmids for PKD1 and PKD2. For 1-liter HEK 293F cell culture, the two plasmids, each of ~1.5 mg, were premixed with 4-mg linear polyethylenimines (PEIs) (Polysciences) in 50-ml fresh medium for 15 to 30 min. The mixture was then added into cell culture followed by 15-min incubation. The transfected cells were cultured at 37°C for 24 hours and then at 30°C for an additional 48 hours.

The cells were harvested by centrifugation at 800g for 10 min and resuspended in the lysis buffer containing 20 mM HEPES, pH 7.5, 150 mM NaCl, 10% glycerol, 5 mM EDTA, and protease inhibitor cocktail (Amresco; 2 µg/ml aprotinin, 2 µg/ml leupeptin, 2 µg/ml pepstatin). The suspension was frozen in liquid nitrogen and stored at -80°C for further experiments.

For protein purification, the thawed suspension was supplemented with 1 mM PMSF prior

to homogenization. The lysate was incubated in the buffer containing 2% DDM (Anatrace), 0.5% soybean lipids (Sigma), and 0.4% CHS (Anatrace) at 4°C for 1.5 to 2 hours for membrane protein extraction. After ultracentrifugation at 18,700g for 40 to 60 min, the supernatant was collected and applied to the anti-FLAG M2 affinity gel (Sigma) at 4°C for three times. The resin was rinsed four times, each with 5 ml of buffer containing 20 mM HEPES, pH 7.5, 150 mM NaCl, 10% glycerol (w/v), 0.06% digitonin (w/v, Sigma), and the aforementioned protease inhibitor cocktail. The proteins were then eluted with wash buffer plus 300 to 400 µg/ml FLAG peptide. The eluent from the anti-FLAG M2 column was subsequently loaded to the Strep-Tactin resin (IBA) and incubated at 4°C for 1 hour. The resin was washed extensively by the same wash buffer before being eluted with wash buffer plus 5 mM D-Desthiobiotin (IBA). The protein eluent was concentrated by a 50-kDa cut-off Centricon (Millipore) and further purified by Superose-6 Increase column (GE Healthcare) in the buffer containing 20 mM HEPES, pH 7.5, 150 mM NaCl, and 0.1% digitonin. The peak fractions corre-

sponding to the PKD1-PKD2 complex were pooled, concentrated, and supplemented with 5 mM EDTA. A typical final yield of the homogeneous complex through this procedure was approximately 2 to 3 µg per liter cell culture.

#### Cryo-EM data acquisition

Holey carbon grids (Quantifoil Au 300 mesh, R1.2/1.3) were glow-discharged in the Plasma Cleaner PDC-32G-2 (HARRICK PLASMA Company) with a vacuum for 2 min and mid force for 22 s. Aliquots (3 µl) of purified PKD1-PKD2 complex at concentration of ~10 mg/ml were placed on the glow-discharged grids, which were then blotted for 2.5 to 3.5 s and flash frozen in liquid ethane cooled by liquid nitrogen using Vitrobot Mark IV (Thermo Fisher Scientific) at 8°C and 100% humidity without wait time or blot force.

The grids were transferred to a Titan Krios TEM operated at 300 kV and equipped with Gatan GIF Quantum energy filter and Gatan K2 direct electron detector and Cs corrector. A total of 3761 zero-loss movie stacks were automatically collected using AutoEMation II (developed by J. Lei)

in the super-resolution mode (62) with 20-eV slit in energy filter at a nominal magnification of 105,000 $\times$  with defocus range from -1.0 to -2.0 µm. Each micrograph stack, which contained 32 frames, was exposed for 5.6 s with a total electron dose of ~50 e $^-$ /Å $^2$ . The stacks were motion corrected using MotionCor2 (63) with a binning factor of 2, resulting in a pixel size of 1.091 Å. Dose weighting was performed concurrently (64). The defocus values were estimated with Gctf (65).

#### Cryo-EM image processing

The procedure for image processing of PKD1-PKD2 complex is presented in fig. S3. A total of 902,194 particles were automatically picked with Gautomatch (developed by Kai Zhang, <https://www.mrc-lmb.cam.ac.uk/kzhang/Gautomatch/>). After 2D classification, 467,705 good particles were selected and subjected to 3D classification. The PKD2 map (EMDB ID: 8354) was low-pass filtered to 10 Å to be used as the initial model (4). All the particles were first subjected to global angular search 3D classification using RELION 2.0 with one class and step size of 7.5°. For each of the last several iterations of the global angular search 3D classification, a local angular search 3D classification was executed with class number being 8 or 15, step size of 3.75°, and local search range of 15°. A total of 210,935 good particles were combined and subjected to further 3D classification, from which 116,485 good particles were selected and subjected to 3D auto-refinement, resulting in a final resolution at 3.2 Å. To further improve the map quality for the flexible PKD2 III subunit, a total of 27,296 particles were selected by applying a mask during the “skip alignment” 3D classification, yielding a map with better S6a area with an overall resolution of 3.6 Å.

All resolutions mentioned above are determined according to the gold-standard Fourier shell correlation 0.143 criterion and with a high-resolution noise substitution method (66).

#### Model building and structure refinement

The PKD2 structure (PDB code: 5T4D) (4) was docked into the 3.2-Å map for model building of the majority of PKD1-CTD and PKD2 subunits in the complex. The VSD and TOP domains of PKD2 III, as well as the S5 and S6a of PKD1, were built based on the 3.6-Å map wherein these regions were better resolved. The secondary structural elements of PKD1-NTD were predicted in I-TASSER (38). Bulky residues (Phe, Trp, Arg, Lys, and Tyr) were used as reference for sequence assignment. Owing to the relatively poor resolutions, only poly-Ala chain was built for the PLAT domain taking account of the prediction from I-TASSER (38). The built model was real space refined using PHENIX with geometry restraints applied (67). The whole process was monitored to avoid overfitting by executing model refinements in two independent half maps, following the gold-standard refinement approach, and testing against each other (67). The final model was evaluated using MolProbity (68). The statistics

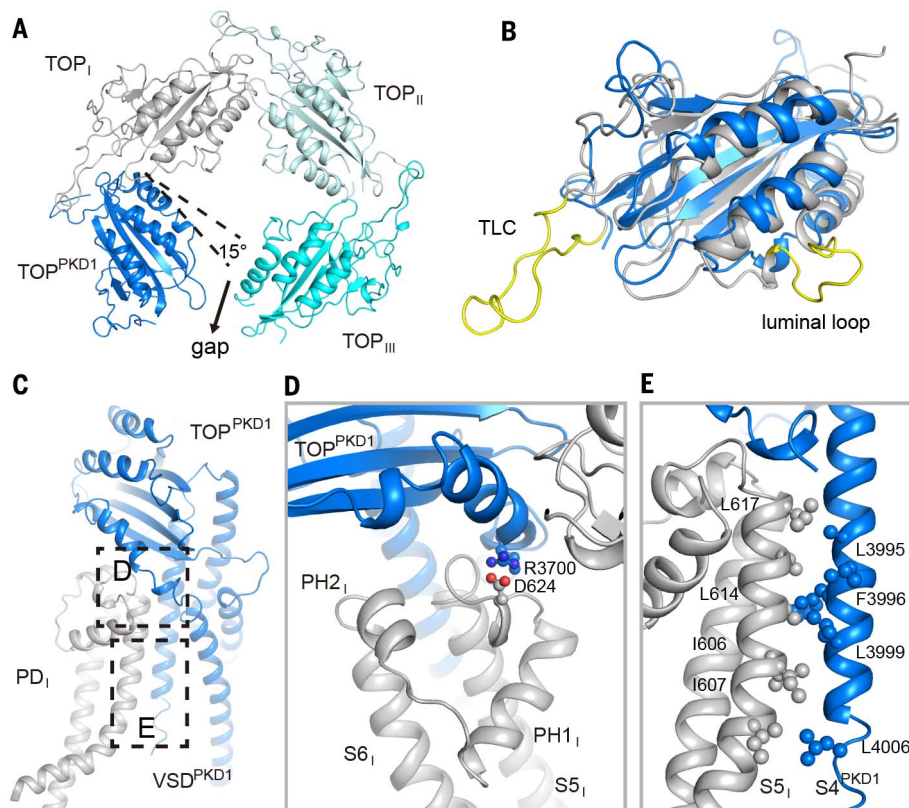


**Fig. 5. Interactions between PKD1 and PKD2.** (A) The ring of TOP domains in the heterotetramer is gapped owing to the deviation of TOP<sub>PKD1</sub> from the fourfold symmetry. Shown is an extracellular view. (B) Structural comparison of TOP<sub>PKD1</sub> and TOP<sub>PKD2</sub>. The elements that mediate interactions among TOP domains in PKD2 (gray) but are missing (luminal loop) or invisible (TLC) in TOP<sub>PKD1</sub> (blue) are colored yellow. (C) Two additional interfaces between PKD1 and PKD2. The indicated interfaces are illustrated in detail in (D) and (E). (D) The electrostatic interaction between TOP<sub>PKD1</sub> and PD<sub>I</sub>. (E) A hydrophobic interface between S5<sub>I</sub> and S4<sub>PKD1</sub>. This interface observes the canonical domain-swapped folding principle of VGICs. The interface residues are shown as spheres.

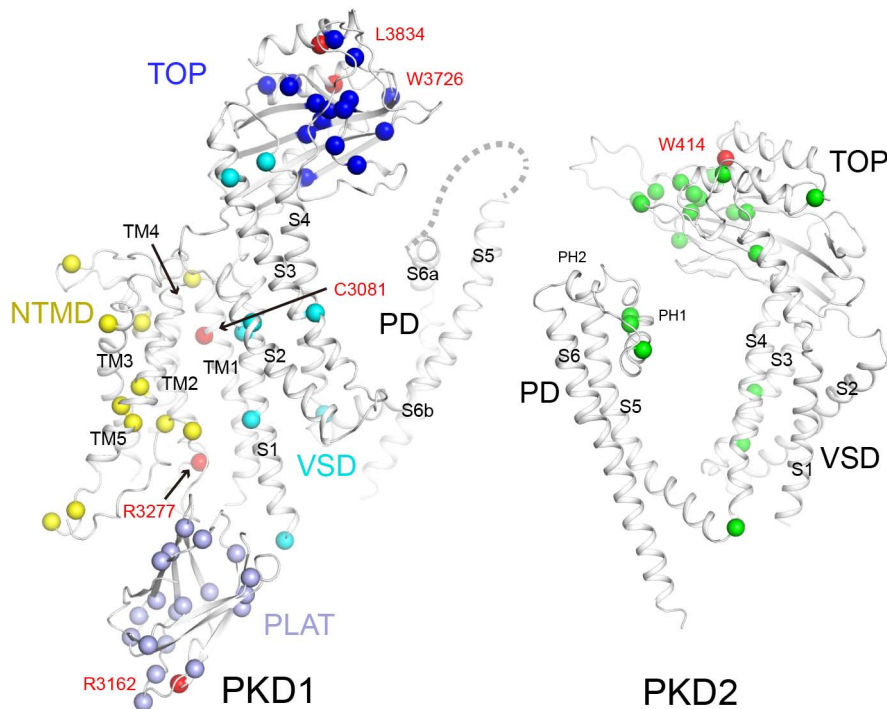


**Fig. 6. Structural mapping of ADPKD mutations.** The  $\alpha$  carbon atoms of representative disease-related residues are shown as spheres and are domain colored. The missense mutations were summarized from the ADPKD Mutation Database (<http://pkdb.mayo.edu/>).

for data collection and model building and refinement are listed in table S1.

#### Quantitative proteomic analysis by label-free MS

Both full-length and truncated PKD1-PKD2 complexes were overexpressed and purified with the same protocol as mentioned above. Individual proteins were separated by SDS-PAGE followed by in-gel digestion for subsequent MS analysis. Briefly, all the proteins were treated with 25 mM dithiothreitol (DTT) to reduce disulfide bonds and then alkylated with 55 mM iodoacetamide. In-gel digestion was performed using sequencing grade-modified trypsin in 50 mM ammonium bicarbonate at 37°C overnight. The peptides were extracted twice with 1% trifluoroacetic acid in 50% acetonitrile aqueous solution for 30 min. The peptide extracts were then centrifuged in a SpeedVac to reduce the volume.

For LC-MS analysis, peptides were separated by a 60-min gradient elution at a flow rate of 0.300  $\mu$ l/min with a Thermo-Dionex Ultimate 3000 HPLC system, which was directly interfaced with a Thermo LTQ-Orbitrap Velos pro mass spectrometer. The analytical column was a home-made fused silica capillary column (75  $\mu$ m ID, 150 mm in length; Upchurch, Oak Harbor, WA) packed with C-18 resin (300 A, 5  $\mu$ m; Varian, Lexington, MA). Mobile phase A contained 0.1% formic acid, and mobile phase B contained 100% acetonitrile supplemented with 0.1% formic acid. An LTQ-Orbitrap mass spectrometer was oper-

ated in the data-dependent acquisition mode using Xcalibur 2.0.7 software. A single full-scan mass spectrum in the Orbitrap (400 to 1800 m/z, 30,000 resolution) was followed by 20 data-dependent MS/MS scans in an ion trap at 35% normalized collision energy (CID).

The raw data were analyzed by MaxQuant (version 1.6.2.3) (69) using standard settings with the additional options to match between runs (between triplicates) with LFQ and iBAQ selected. The generated “proteingroups.txt” table was filtered for contaminants, reverse hits, number of unique peptides (>0) and number of peptides (>1) in Perseus (from MaxQuant package). To determine the stoichiometry of the target complexes, we compared the relative abundance of the identified interactors as measured by the iBAQ intensities (35). The sequences (PKD1 residues 3049 to 4169 and PKD2 residues 185 to 723) were used to search against both full-length and truncated samples to estimate the stoichiometry of the transmembrane domains. The data are listed in table S2.

#### Confocal microscopy immunofluorescence imaging

HEK 293T cells transfected with DNA combinations indicated in fig. S1 and Lipofectamine LTX with Plus (Invitrogen) were incubated for 24 hours. Cells were washed twice with PBS solution and then fixed with 4% paraformaldehyde in PBS for 15 min. After a 5-min wash with PBS for three times, the cells were either permeabilized with 0.5% Triton X-100 in TBS (25 mM

Tris-HCl, pH 7.5, and 150 mM NaCl) for 20 min followed by three 5-min washes or processed without Triton X-100. The treated cells were then blocked with 4% bovine serum albumin (BSA) in TBS for 1 hour and incubated with the polyclonal anti-FLAG antibody in the same blocking solution at room temperature for 1 hour. After three 10-min washes with TBS, the cells were incubated with fluorescein (FITC)-conjugated goat anti-rabbit IgG in 4% BSA at room temperature for 1 hour. After another three 10-min washes with TBS, cells were mounted on slides and imaged with a confocal microscope.

The confocal fluorescence imaging experiments were performed with a ZEISS laser scanning confocal microscopy (LSM710). Data were collected and analyzed by ZEN 2012 Light Edition software.

#### REFERENCES AND NOTES

- V. E. Torres, P. C. Harris, Y. Pirson, Autosomal dominant polycystic kidney disease. *Lancet* **369**, 1287–1301 (2007). doi: [10.1016/S0140-6736\(07\)60601-1](https://doi.org/10.1016/S0140-6736(07)60601-1); pmid: [17434405](https://pubmed.ncbi.nlm.nih.gov/17434405/)
- P. C. Harris, V. E. Torres, Polycystic kidney disease. *Annu. Rev. Med.* **60**, 321–337 (2009). doi: [10.1146/annurev.med.60.101707.125712](https://doi.org/10.1146/annurev.med.60.101707.125712); pmid: [18947299](https://pubmed.ncbi.nlm.nih.gov/18947299/)
- P. Igarashi, S. Somlo, Polycystic kidney disease. *J. Am. Soc. Nephrol.* **18**, 1371–1373 (2007). doi: [10.1681/ASN.2007030299](https://doi.org/10.1681/ASN.2007030299); pmid: [17429047](https://pubmed.ncbi.nlm.nih.gov/17429047/)
- P. S. Shen et al., The structure of the polycystic kidney disease channel PKD2 in lipid nanodiscs. *Cell* **167**, 763–773.e11 (2016). doi: [10.1016/j.cell.2016.09.048](https://doi.org/10.1016/j.cell.2016.09.048); pmid: [27768895](https://pubmed.ncbi.nlm.nih.gov/27768895/)
- W. Zheng et al., Hydrophobic pore gates regulate ion permeation in polycystic kidney disease 2 and 2L1 channels. *Nat. Commun.* **9**, 2302 (2018). doi: [10.1038/s41467-018-04586-x](https://doi.org/10.1038/s41467-018-04586-x); pmid: [29899465](https://pubmed.ncbi.nlm.nih.gov/29899465/)
- J. Zhou, Polycystins and primary cilia: Primers for cell cycle progression. *Annu. Rev. Physiol.* **71**, 83–113 (2009). doi: [10.1146/annurev.physiol.70.110006.100621](https://doi.org/10.1146/annurev.physiol.70.110006.100621); pmid: [19572811](https://pubmed.ncbi.nlm.nih.gov/19572811/)
- J. Hughes et al., The polycystic kidney disease 1 (PKD1) gene encodes a novel protein with multiple cell recognition domains. *Nat. Genet.* **10**, 151–160 (1995). doi: [10.1038/ng095-151](https://doi.org/10.1038/ng095-151); pmid: [7663510](https://pubmed.ncbi.nlm.nih.gov/7663510/)
- T. Mochizuki et al., PKD2, a gene for polycystic kidney disease that encodes an integral membrane protein. *Science* **272**, 1339–1342 (1996). doi: [10.1126/science.272.5266.1339](https://doi.org/10.1126/science.272.5266.1339); pmid: [8650545](https://pubmed.ncbi.nlm.nih.gov/8650545/)
- A. Patel, E. Honoré, Polycystins and renovascular mechanosensory transduction. *Nat. Rev. Nephrol.* **6**, 530–538 (2010). doi: [10.1038/nrneph.2010.97](https://doi.org/10.1038/nrneph.2010.97); pmid: [20625375](https://pubmed.ncbi.nlm.nih.gov/20625375/)
- S. Kim et al., The polycystin complex mediates Wnt/ $\text{Ca}^{2+}$  signaling. *Nat. Cell Biol.* **18**, 752–764 (2016). doi: [10.1038/ncb3363](https://doi.org/10.1038/ncb3363); pmid: [27214281](https://pubmed.ncbi.nlm.nih.gov/27214281/)
- S. M. Nauli et al., Polycystins 1 and 2 mediate mechanosensation in the primary cilium of kidney cells. *Nat. Genet.* **33**, 129–137 (2003). doi: [10.1038/ng1076](https://doi.org/10.1038/ng1076); pmid: [12514735](https://pubmed.ncbi.nlm.nih.gov/12514735/)
- V. Chauvet et al., Mechanical stimuli induce cleavage and nuclear translocation of the polycystin-1 C terminus. *J. Clin. Invest.* **114**, 1433–1443 (2004). doi: [10.1172/JCI21753](https://doi.org/10.1172/JCI21753); pmid: [15545994](https://pubmed.ncbi.nlm.nih.gov/15545994/)
- Y. Yang, B. E. Ehrlich, Structural studies of the C-terminal tail of polycystin-2 (PC2) reveal insights into the mechanisms used for the functional regulation of PC2. *J. Physiol.* **594**, 4141–4149 (2016). doi: [10.1113/JP270933](https://doi.org/10.1113/JP270933); pmid: [26857659](https://pubmed.ncbi.nlm.nih.gov/26857659/)
- L. Geng et al., Distribution and developmentally regulated expression of murine polycystin. *Am. J. Physiol.* **272**, F451–F459 (1997). pmid: [9140045](https://pubmed.ncbi.nlm.nih.gov/9140045/)
- C. J. Ward et al., Polycystin, the polycystic kidney disease 1 protein, is expressed by epithelial cells in fetal, adult, and polycystic kidney. *Proc. Natl. Acad. Sci. U.S.A.* **93**, 1524–1528 (1996). doi: [10.1073/pnas.93.4.1524](https://doi.org/10.1073/pnas.93.4.1524); pmid: [8643665](https://pubmed.ncbi.nlm.nih.gov/8643665/)
- L. Foggensteiner et al., Cellular and subcellular distribution of polycystin-2, the protein product of the PKD2 gene. *J. Am. Soc. Nephrol.* **11**, 814–827 (2000). pmid: [10770959](https://pubmed.ncbi.nlm.nih.gov/10770959/)
- K. Hanaka et al., Co-assembly of polycystin-1 and -2 produces unique cation-permeable currents. *Nature* **408**, 990–994 (2000). doi: [10.1038/35050128](https://doi.org/10.1038/35050128); pmid: [11140688](https://pubmed.ncbi.nlm.nih.gov/11140688/)
- M. Delling et al., Primary cilia are not calcium-responsive mechanosensors. *Nature* **531**, 656–660 (2016). doi: [10.1038/nature17426](https://doi.org/10.1038/nature17426); pmid: [27007841](https://pubmed.ncbi.nlm.nih.gov/27007841/)

19. F. Qian et al., PKD1 interacts with PKD2 through a probable coiled-coil domain. *Nat. Genet.* **16**, 179–183 (1997). doi: [10.1038/ng0697-179](https://doi.org/10.1038/ng0697-179); pmid: [9171830](https://pubmed.ncbi.nlm.nih.gov/9171830/)
20. L. Tsikas, E. Kim, T. Arnould, V. P. Sukhatme, G. Walz, Homodimeric interactions between the gene products of *PKD1* and *PKD2*. *Proc. Natl. Acad. Sci. U.S.A.* **94**, 6965–6970 (1997). doi: [10.1073/pnas.94.13.6965](https://doi.org/10.1073/pnas.94.13.6965); pmid: [9192675](https://pubmed.ncbi.nlm.nih.gov/9192675/)
21. Y. Yu et al., Structural and molecular basis of the assembly of the TRPP2/PKD1 complex. *Proc. Natl. Acad. Sci. U.S.A.* **106**, 11558–11563 (2009). doi: [10.1073/pnas.0903684106](https://doi.org/10.1073/pnas.0903684106); pmid: [19556541](https://pubmed.ncbi.nlm.nih.gov/19556541/)
22. J. Zhu et al., Structural model of the TRPP2/PKD1 C-terminal coiled-coil complex produced by a combined computational and experimental approach. *Proc. Natl. Acad. Sci. U.S.A.* **108**, 10133–10138 (2011). doi: [10.1073/pnas.101769108](https://doi.org/10.1073/pnas.101769108); pmid: [21642537](https://pubmed.ncbi.nlm.nih.gov/21642537/)
23. V. Babich et al., The N-terminal extracellular domain is required for polycystin-1-dependent channel activity. *J. Biol. Chem.* **279**, 25582–25589 (2004). doi: [10.1074/jbc.M402829200](https://doi.org/10.1074/jbc.M402829200); pmid: [15060061](https://pubmed.ncbi.nlm.nih.gov/15060061/)
24. S. Feng et al., Identification and functional characterization of an N-terminal oligomerization domain for polycystin-2. *J. Biol. Chem.* **283**, 28471–28479 (2008). doi: [10.1074/jbc.M803834200](https://doi.org/10.1074/jbc.M803834200); pmid: [18701462](https://pubmed.ncbi.nlm.nih.gov/18701462/)
25. Y. Cai et al., Altered trafficking and stability of polycystins underlie polycystic kidney disease. *J. Clin. Invest.* **124**, 5129–5144 (2014). doi: [10.1172/JCI67273](https://doi.org/10.1172/JCI67273); pmid: [23565220](https://pubmed.ncbi.nlm.nih.gov/23565220/)
26. Q. Su et al., Cryo-EM structure of the polycystic kidney disease-like channel PKD2L1. *Nat. Commun.* **9**, 1192 (2018). doi: [10.1038/s41467-018-03606-0](https://doi.org/10.1038/s41467-018-03606-0); pmid: [29567962](https://pubmed.ncbi.nlm.nih.gov/29567962/)
27. M. Grieben et al., Structure of the polycystic kidney disease TRP channel polycystin-2 (PC2). *Nat. Struct. Mol. Biol.* **24**, 114–122 (2017). doi: [10.1038/nsmb.3343](https://doi.org/10.1038/nsmb.3343); pmid: [27991905](https://pubmed.ncbi.nlm.nih.gov/27991905/)
28. M. Wilkes et al., Molecular insights into lipid-assisted Ca<sup>2+</sup> regulation of the TRP channel polycystin-2. *Nat. Struct. Mol. Biol.* **24**, 123–130 (2017). doi: [10.1038/nsmb.3357](https://doi.org/10.1038/nsmb.3357); pmid: [28092368](https://pubmed.ncbi.nlm.nih.gov/28092368/)
29. K. Venkatachalam, C. Montell, TRP channels. *Annu. Rev. Biochem.* **76**, 387–417 (2007). doi: [10.1146/annurev.biochem.75.103004.142819](https://doi.org/10.1146/annurev.biochem.75.103004.142819); pmid: [17579562](https://pubmed.ncbi.nlm.nih.gov/17579562/)
30. M. Bycroft et al., The structure of a PKD domain from polycystin-1: Implications for polycystic kidney disease. *EMBO J.* **18**, 297–305 (1999). doi: [10.1093/emboj/18.2.297](https://doi.org/10.1093/emboj/18.2.297); pmid: [9889186](https://pubmed.ncbi.nlm.nih.gov/9889186/)
31. Y. Xu et al., The polycystin-1, lipoxigenase, and α-toxin domain regulates polycystin-1 trafficking. *J. Am. Soc. Nephrol.* **27**, 1159–1173 (2016). doi: [10.1681/ASN.201411074](https://doi.org/10.1681/ASN.201411074); pmid: [26311459](https://pubmed.ncbi.nlm.nih.gov/26311459/)
32. A. Bateman, R. Sandford, The PLAT domain: A new piece in the PKD1 puzzle. *Curr. Biol.* **9**, R588–R590 (1999). doi: [10.1016/S0960-9822\(99\)80380-7](https://doi.org/10.1016/S0960-9822(99)80380-7); pmid: [10469604](https://pubmed.ncbi.nlm.nih.gov/10469604/)
33. D. H. Grimm et al., Polycystin-1 distribution is modulated by polycystin-2 expression in mammalian cells. *J. Biol. Chem.* **278**, 36786–36793 (2003). doi: [10.1074/jbc.M306536200](https://doi.org/10.1074/jbc.M306536200); pmid: [12840011](https://pubmed.ncbi.nlm.nih.gov/12840011/)
34. P. B. Rosenthal, R. Henderson, Optimal determination of particle orientation, absolute hand, and contrast loss in single-particle electron cryomicroscopy. *J. Mol. Biol.* **333**, 721–745 (2003). doi: [10.1016/j.jmb.2003.07.013](https://doi.org/10.1016/j.jmb.2003.07.013); pmid: [14568533](https://pubmed.ncbi.nlm.nih.gov/14568533/)
35. A. H. Smits, P. W. Jansen, I. Poser, A. A. Hyman, M. Vermeulen, Stoichiometry of chromatin-associated protein complexes revealed by label-free quantitative mass spectrometry-based proteomics. *Nucleic Acids Res.* **41**, e28 (2013). doi: [10.1093/nar/gks941](https://doi.org/10.1093/nar/gks941); pmid: [23066101](https://pubmed.ncbi.nlm.nih.gov/23066101/)
36. R. van Nuland et al., Quantitative dissection and stoichiometry determination of the human SET1/MLL histone methyltransferase complexes. *Mol. Cell. Biol.* **33**, 2067–2077 (2013). doi: [10.1128/MCB.01742-12](https://doi.org/10.1128/MCB.01742-12); pmid: [23508102](https://pubmed.ncbi.nlm.nih.gov/23508102/)
37. C. Smacznak et al., Proteomics-based identification of low-abundance signaling and regulatory protein complexes in native plant tissues. *Nat. Protoc.* **7**, 2144–2158 (2012). doi: [10.1038/nprot.2012.129](https://doi.org/10.1038/nprot.2012.129); pmid: [23196971](https://pubmed.ncbi.nlm.nih.gov/23196971/)
38. J. Yang et al., The I-TASSER Suite: Protein structure and function prediction. *Nat. Methods* **12**, 7–8 (2015). doi: [10.1038/nmeth.3213](https://doi.org/10.1038/nmeth.3213); pmid: [25549265](https://pubmed.ncbi.nlm.nih.gov/25549265/)
39. U. A. Hellmich, R. Gaudet, Structural biology of TRP channels. *Handb. Exp. Pharmacol.* **223**, 963–990 (2014). doi: [10.1007/978-3-319-05161-1\\_10](https://doi.org/10.1007/978-3-319-05161-1_10); pmid: [24961976](https://pubmed.ncbi.nlm.nih.gov/24961976/)
40. W. A. Catterall, Forty years of sodium channels: Structure, function, pharmacology, and epilepsy. *Neurochem. Res.* **42**, 2495–2504 (2017). doi: [10.1007/s11064-017-2314-9](https://doi.org/10.1007/s11064-017-2314-9); pmid: [28589518](https://pubmed.ncbi.nlm.nih.gov/28589518/)
41. E. Grandi et al., Potassium channels in the heart: Structure, function and regulation. *J. Physiol.* **595**, 2209–2228 (2017). doi: [10.1113/JP272864](https://doi.org/10.1113/JP272864); pmid: [27861921](https://pubmed.ncbi.nlm.nih.gov/27861921/)
42. L. Holm, L. M. Laakso, DALI server update. *Nucleic Acids Res.* **44**, W351–W356 (2016). doi: [10.1093/nar/gkw357](https://doi.org/10.1093/nar/gkw357); pmid: [27131377](https://pubmed.ncbi.nlm.nih.gov/27131377/)
43. S. Rossetti et al., Identification of gene mutations in autosomal dominant polycystic kidney disease through targeted resequencing. *J. Am. Soc. Nephrol.* **23**, 915–933 (2012). doi: [10.1681/ASN.201101032](https://doi.org/10.1681/ASN.201101032); pmid: [22383692](https://pubmed.ncbi.nlm.nih.gov/22383692/)
44. X. Zhou et al., Cryo-EM structures of the human endolyosomal TRPML3 channel in three distinct states. *Nat. Struct. Mol. Biol.* **24**, 1146–1154 (2017). doi: [10.1038/nsmb.3502](https://doi.org/10.1038/nsmb.3502); pmid: [29106414](https://pubmed.ncbi.nlm.nih.gov/29106414/)
45. Z. Salehi-Najafabadi et al., Extracellular loops are essential for the assembly and function of polycystin receptor-ion channel complexes. *J. Biol. Chem.* **292**, 4210–4221 (2017). doi: [10.1074/jbc.M116.767897](https://doi.org/10.1074/jbc.M116.767897); pmid: [28154010](https://pubmed.ncbi.nlm.nih.gov/28154010/)
46. K. Hoppe et al., Functional polycystin-1 dosage governs autosomal dominant polycystic kidney disease severity. *J. Clin. Invest.* **122**, 4257–4273 (2012). doi: [10.1172/JCI64313](https://doi.org/10.1172/JCI64313); pmid: [23064367](https://pubmed.ncbi.nlm.nih.gov/23064367/)
47. J. Hoefele, K. Mayer, M. Scholz, H. G. Klein, Novel PKD1 and PKD2 mutations in autosomal dominant polycystic kidney disease (ADPKD). *Nephrol. Dial. Transplant.* **26**, 2181–2188 (2011). doi: [10.1093/ndt/gfq720](https://doi.org/10.1093/ndt/gfq720); pmid: [21115670](https://pubmed.ncbi.nlm.nih.gov/21115670/)
48. S. Rossetti et al., Comprehensive molecular diagnostics in autosomal dominant polycystic kidney disease. *J. Am. Soc. Nephrol.* **18**, 2143–2160 (2007). doi: [10.1681/ASN.2006121387](https://doi.org/10.1681/ASN.2006121387); pmid: [17582161](https://pubmed.ncbi.nlm.nih.gov/17582161/)
49. G. Aguiari et al., Novel splicing and missense mutations in autosomal dominant polycystic kidney disease 1 (*PKD1*) gene: Expression of mutated genes. *Hum. Mutat.* **16**, 444–445 (2000). doi: [10.1002/1098-1004\(200011\)16:5<444::AID-HUMU11>3.0.CO;2-C](https://doi.org/10.1002/1098-1004(200011)16:5<444::AID-HUMU11>3.0.CO;2-C); pmid: [11058904](https://pubmed.ncbi.nlm.nih.gov/11058904/)
50. B. Reed et al., Presence of de novo mutations in autosomal dominant polycystic kidney disease patients without family history. *Am. J. Kidney Dis.* **52**, 1042–1050 (2008). doi: [10.1053/j.ajkd.2008.05.015](https://doi.org/10.1053/j.ajkd.2008.05.015); pmid: [18640754](https://pubmed.ncbi.nlm.nih.gov/18640754/)
51. S. Rossetti et al., A complete mutation screen of the ADPKD genes by DHPLC. *Kidney Int.* **61**, 1588–1599 (2002). doi: [10.1046/j.1523-1755.2002.00326.x](https://doi.org/10.1046/j.1523-1755.2002.00326.x); pmid: [12196708](https://pubmed.ncbi.nlm.nih.gov/12196708/)
52. Y. C. Tan et al., Novel method for genomic analysis of *PKD1* and *PKD2* mutations in autosomal dominant polycystic kidney disease. *Hum. Mutat.* **30**, 264–273 (2009). doi: [10.1002/humu.20842](https://doi.org/10.1002/humu.20842); pmid: [19837007](https://pubmed.ncbi.nlm.nih.gov/19837007/)
53. X. Liu et al., Polycystin-2 is an essential ion channel subunit in the primary cilium of the renal collecting duct epithelium. *eLife* **7**, e33183 (2018). doi: [10.7554/elife.33183](https://doi.org/10.7554/elife.33183); pmid: [29443690](https://pubmed.ncbi.nlm.nih.gov/29443690/)
54. Y. Yu et al., Molecular mechanism of the assembly of an acid-sensing receptor ion channel complex. *Nat. Commun.* **3**, 1252 (2012). doi: [10.1038/ncomms2257](https://doi.org/10.1038/ncomms2257); pmid: [2321238](https://pubmed.ncbi.nlm.nih.gov/2321238)
55. S. Bataille, Y. Berland, M. Fontes, S. Burtey, High resolution melt analysis for mutation screening in *PKD1* and *PKD2*. *BMC Nephrol.* **12**, 57 (2011). doi: [10.1186/1471-2369-12-57](https://doi.org/10.1186/1471-2369-12-57); pmid: [22008521](https://pubmed.ncbi.nlm.nih.gov/22008521/)
56. L. Ding et al., Novel mutations of *PKD1* gene in Chinese patients with autosomal dominant polycystic kidney disease. *Nephrol. Dial. Transplant.* **17**, 75–80 (2002). doi: [10.1093/ndt/17.1.75](https://doi.org/10.1093/ndt/17.1.75); pmid: [12173467](https://pubmed.ncbi.nlm.nih.gov/12173467/)
57. M. Ma, A. R. Gallagher, S. Somlo, Ciliary mechanisms of cyst formation in polycystic kidney disease. *Cold Spring Harb. Perspect. Biol.* **9**, a028209 (2017). doi: [10.1101/cshperspect.a028209](https://doi.org/10.1101/cshperspect.a028209); pmid: [28320755](https://pubmed.ncbi.nlm.nih.gov/28320755/)
58. S. J. Kleene, N. K. Kleene, The native TRPP2-dependent channel of murine renal primary cilia. *Am. J. Physiol. Renal Physiol.* **312**, F96–F108 (2017). doi: [10.1152/ajprenal.00272.2016](https://doi.org/10.1152/ajprenal.00272.2016); pmid: [27760766](https://pubmed.ncbi.nlm.nih.gov/27760766/)
59. T. Matsuda, C. L. Cepko, Electroporation and RNA interference in the rodent retina *in vivo* and *in vitro*. *Proc. Natl. Acad. Sci. U.S.A.* **101**, 16–22 (2004). doi: [10.1073/pnas.2235688101](https://doi.org/10.1073/pnas.2235688101); pmid: [15403031](https://pubmed.ncbi.nlm.nih.gov/15403031/)
60. C. J. Gloeckner, K. Boldt, A. Schumacher, M. Ueffing, Tandem affinity purification of protein complexes from mammalian cells by the Strep/FLAG (SF)-TAP tag. *Methods Mol. Biol.* **564**, 359–372 (2009). doi: [10.1007/978-1-60761-157-8\\_21](https://doi.org/10.1007/978-1-60761-157-8_21); pmid: [19544034](https://pubmed.ncbi.nlm.nih.gov/19544034/)
61. C. J. Gloeckner, K. Boldt, M. Ueffing, Strep/FLAG tandem affinity purification (SF-TAP) to study protein interactions. *Curr. Protoc. Protein Sci.* **57**, 19.20.1–19.20.19 (2009). doi: [10.1007/978-1-60761-157-8\\_21](https://doi.org/10.1007/978-1-60761-157-8_21); pmid: [19544034](https://pubmed.ncbi.nlm.nih.gov/19544034/)
62. J. Lei, J. Frank, Automated acquisition of cryo-electron micrographs for single particle reconstruction on an FEI Tecnai electron microscope. *J. Struct. Biol.* **150**, 69–80 (2005). doi: [10.1016/j.jsb.2005.01.002](https://doi.org/10.1016/j.jsb.2005.01.002); pmid: [15797731](https://pubmed.ncbi.nlm.nih.gov/15797731/)
63. S. Q. Zheng et al., MotionCor2: Anisotropic correction of beam-induced motion for improved cryo-electron microscopy. *Nat. Methods* **14**, 331–332 (2017). pmid: [28250466](https://pubmed.ncbi.nlm.nih.gov/28250466/)
64. T. Grant, N. Grigorieff, Measuring the optimal exposure for single particle cryo-EM using a 2.6 Å reconstruction of rotavirus VP6. *eLife* **4**, e06980 (2015). doi: [10.7554/eLife.06980](https://doi.org/10.7554/eLife.06980); pmid: [26023829](https://pubmed.ncbi.nlm.nih.gov/26023829/)
65. K. Zhang, Gctt, Real-time CTF determination and correction. *J. Struct. Biol.* **193**, 1–12 (2016). doi: [10.1016/j.jsb.2015.11.003](https://doi.org/10.1016/j.jsb.2015.11.003); pmid: [26592709](https://pubmed.ncbi.nlm.nih.gov/26592709/)
66. S. Chen et al., High-resolution noise substitution to measure overfitting and validate resolution in 3D structure determination by single particle electron cryomicroscopy. *Ultramicroscopy* **135**, 24–35 (2013). doi: [10.1016/j.ultrami.2013.06.004](https://doi.org/10.1016/j.ultrami.2013.06.004); pmid: [23872039](https://pubmed.ncbi.nlm.nih.gov/23872039/)
67. P. D. Adams et al., PHENIX: A comprehensive Python-based system for macromolecular structure solution. *Acta Crystallogr. D Biol. Crystallogr.* **66**, 213–221 (2010). pmid: [20124702](https://pubmed.ncbi.nlm.nih.gov/20124702/)
68. V. B. Chen et al., MolProbity: All-atom structure validation for macromolecular crystallography. *Acta Crystallogr. D Biol. Crystallogr.* **66**, 12–21 (2010). doi: [10.1107/S0907444909042073](https://doi.org/10.1107/S0907444909042073); pmid: [20057044](https://pubmed.ncbi.nlm.nih.gov/20057044/)
69. J. Cox, M. Mann, MaxQuant enables high peptide identification rates, individualized p.p.b.-range mass accuracies and proteome-wide protein quantification. *Nat. Biotechnol.* **26**, 1367–1372 (2008). doi: [10.1038/nbt.1511](https://doi.org/10.1038/nbt.1511); pmid: [19029910](https://pubmed.ncbi.nlm.nih.gov/19029910/)
70. N. Alexander, N. Woetzel, J. Meiler, bcl:Cluster: A method for clustering biological molecules coupled with visualization in the PyMol Molecular Graphics System. *IEEE Int. Conf. Comput. Adv. Bio. Med. Sci.* **2011**, 13–18 (2011). pmid: [27818847](https://pubmed.ncbi.nlm.nih.gov/27818847/)

Downloaded from https://www.science.org at University of Georgia on August 19, 2024

ACKNOWLEDGMENTS

We thank C. Yan and J. Zeng for advice on model building; Xiaomin Li, Xiaomei Li, and X. Hu for technical support during cryo-EM data collection; H. Deng and X. Meng at the Center of Biomedical Analysis, Tsinghua University, for MS analysis; and C. Huang and S. Gao at Peking University for advice on MS analysis. We thank the Tsinghua University Branch of China National Center for Protein Sciences (Beijing) for providing the facility support. The computation was completed on the “Explorer 100” cluster system of Tsinghua National Laboratory for Information Science and Technology. **Funding:** This work was supported by funds from the National Natural Science Foundation of China (31621092, 31430020, 81370784, and 81770659) and the National Key R&D Program (grant 2016YFA050100) from the Ministry of Science and Technology of China. **Author contributions:** Y.S., C.M., S.Y., and T.W. conceived the project; Y.S., Q.S., and F.H. designed experiments. Q.S., F.H., X.G., and J.L. performed experiments. All authors contributed to data analysis. Y.S., Q.S., and F.H. wrote the manuscript. **Competing interests:** The authors declare no competing interests. **Data and materials availability:** The cryo-EM maps and the structure have been deposited to the Electron Microscopy Data Bank (EMDB 6991 and EMDB 6992) and the Protein Data Bank (PDB 6A70), respectively.

## SUPPLEMENTARY MATERIALS

[www.sciencemag.org/content/361/6406/eaat9819/suppl/DC1](https://www.sciencemag.org/content/361/6406/eaat9819/suppl/DC1)  
 Figs. S1 to S9  
 Tables S1 to S3  
 References (71, 72)  
 24 April 2018; accepted 30 July 2018  
 Published online 9 August 2018  
[10.1126/science.aat9819](https://doi.org/10.1126/science.aat9819)